Large Eddy Simulations of the Flow Around a Square Prism

C. Fureby,[*] G. Tabor,[†] H. G. Weller,[†] and A. D. Gosman[‡]
Imperial College, London, England SW7 2BX, United Kingdom

The aim of this study is to examine unsteady wake flows by means of large eddy simulation (LES). In particular, the flow around a square prism in a channel at a prism-height Reynolds number of 2.14×10^4 is studied using different subgrid scale (SGS) models and different grids. Results from first- and second-order statistical moments of the velocity are validated against two sets of experimental data and compared with different Reynolds-average simulations. All LES models correctly reproduce the first- and second-order statistical moments of the resolvable velocity, the global parameters, such as the lift and drag coefficients and their fluctuations, and the Strouhal number, as well as the length of the recirculation region. However, a locally refined grid is necessary to reproduce the maximum velocity within the recirculation region. LES appears virtually independent of the details of the SGS model if it can correctly channel kinetic energy out of eddies close to the cutoff wave number to prevent aliasing provided that the resolution is fine enough to ensure that the cutoff wave number is within the inertial subrange. In addition, phase-averaged flow quantities are compared with experimental data; this comparison supports the belief in LES as a reliable and accurate model for studying unsteady flows. The LES results are subsequently used to analyze and describe the topology of the flow.

I. Introduction

THE flow around bluff bodies is very complex and can involve regions of laminar, transitional, and turbulent flows, unsteady separation and reattachment associated with the obstacle, and the formation of coherent structures, particularly in the wake region of the flow. The wake is spatially complex, often consisting of curved shear layers enclosing a region of extreme complexity characterized by the presence of intense vortices, but also including the entrainment of irrotational flow elements into the wake from the surroundings. The vortices are generated by shear around the obstacle and are shed and convected down the wake. If the obstacle exhibits a degree of bilateral symmetry, the wake may exhibit self-induced periodicity because of vortices being shed from alternate sides of the obstacle. The second effect of the vortex shedding is the generation of intense fluctuating forces on the obstacle in the streamwise and spanwise directions. Many industrial applications and environmental situations including tall buildings and technical structures such as cooling towers, chimneys and suspension bridges, flame holders in combustion chambers, cooling of electronic equipment and components and flow-metering devices require better predictions of the flow characteristics. These demands, as well as the overall desire to increase our present understanding of the fundamental physical processes governing such flows, demonstrate the need for advanced flow modeling. In this study a square prism mounted in a rectilinear channel is chosen as a natural compactly characterized bluff body, the separation points of which are fixed and known, unlike the case of a cylinder, where the separation points are known to wander in time. An additional advantage of this geometry, as observed in experimental studies,[1,2] is the favorable pressure gradient just prior to separation, resulting in a very thin separating shear layer; effects on shear-layer development caused by initial shear-layer thickness could therefore be neglected.

Direct numerical simulation (DNS) of the Navier–Stokes equations[3] (NSE), in which all eddies down to the dissipation scales are properly simulated, is almost impossible because of the large computational effort in resolving all scales of motion. Thus, the ne-

cessity for other, less computationally expensive but still accurate methods is apparent. In Reynolds-averaged simulation[4] (RAS), all eddies are averaged over to give equations for variables representing the mean flow. These equations are similar to the NSE but contain terms representing the effects of the turbulence on the mean flow that require modeling. The success of RAS is limited because the large eddies responsible for the primary transport are geometry dependent, and experience indicates that RAS often break down when a variety of flows are considered.[5] Large eddy simulation[6] (LES) lies between the extremes of DNS and RAS in resolution and computational cost using modified NSE, in which eddies smaller than the grid spacing are eliminated from the dynamics by low-pass filtering whereas their effect on the resolvable motion is provided by subgrid scale (SGS) models.[7,8] It is clear from the wealth of simulations that the larger the part of the energy spectrum that is resolved the better the predictions. A recent alternative[9] involves solving the NSE by high-resolution monotone algorithms in which nonlinear high-frequency filters are built into the models providing implicit SGS models, and thus explicit SGS can be dispensed with.

The aims of this study are to 1) analyse the predictive capabilities of LES models based on the eddy-viscosity hypothesis in unsteady, isochoric, wake flows; 2) examine the insensitivity of LES models to the specifics of the SGS model; 3) investigate the physics of unsteady wake flow involving separation, streamline curvature, recirculation, unsteady vortex shedding, and large-scale complex flow structures at a moderately high Reynolds number; and moreover 4) generate a database of first- and second-order statistical moments of the velocity for the flow around a square prism at $Re = 2.14 \times 10^4$, which can be used to examine and calibrate conventional RAS models.

II. LES Model

The fluid dynamic model is based on the incompressible NSE (Ref. 3), i.e., conservation of mass and balance of momentum of a linear viscous fluid. In LES the dependent variables are split into grid scale and SGS components $f = \bar{f} + f'$, where $\bar{f} = G * f$ and $G = G(\mathbf{x}, \Delta)$ is the filter kernel. The filtering is ideally required to be distributive, associative, and to commute with differentiation. Convolving the NSE with G, using the commutation relations $[\nabla, G*]f = [(\partial G/\partial \Delta) * f]\text{grad}\,\Delta + (Gf\mathbf{n})_{\partial D}$, where $\mathbf{n}$ is the outward pointing unit normal to ∂D, and $[\partial_t, G*]f = 0$, the LES equations results. The deficit of commutation results in additional terms in the LES equations; however, following Ref. 10, an order-of-magnitude analysis indicates that these are of $\mathcal{O}(\Delta^2)$, whereas the unresolved transport terms are of $\mathcal{O}(\Delta^n)$, where $\frac{4}{3} < n < 2$. Hence, to a first-order approximation the LES equations are

*Research Associate, Department of Mechanical Engineering; currently Senior Researcher, Department of Warheads and Propulsion, FOA Defence Research Establishment, S-17200 Stockholm, Sweden. Member AIAA.
†Research Associate, Department of Mechanical Engineering.
‡Professor, Department of Mechanical Engineering.

$$\mathrm{div}(\bar{v}) = 0$$

$$\partial_t(\bar{v}) + \mathrm{div}(\bar{v} \otimes \bar{v}) = -\mathrm{grad}\,\bar{p} + \mathrm{div}(\bar{S} - B) + \bar{f} \qquad (1)$$

where v is the velocity, p the pressure, $S = 2\nu D$ the viscous stress tensor, ν the physical viscosity, $D = \frac{1}{2}(\mathrm{grad}\,v + \mathrm{grad}\,v^T)$ the rate-of-strain tensor, $B = (\overline{v \otimes v} - \bar{v} \otimes \bar{v})$ the SGS stress tensor, and f the specific body force (assumed negligible when high-Reynolds-number flows are considered). The SGS stress tensor may be decomposed as $B = L + C + R$, where $L = \overline{\bar{v} \otimes \bar{v}} - \bar{v} \otimes \bar{v}$ is the Leonard stress tensor representing the interaction between resolved eddies to form small-scale turbulence, $C = \overline{\bar{v} \otimes v'} + \overline{v' \otimes \bar{v}}$ is the cross-stress tensor representing interactions between resolved and unresolved eddies and may transfer energy in either direction but mainly toward small-scale eddies, and $R = \overline{v' \otimes v'}$ is the Reynolds-stress tensor representing interactions among the unresolved small-scale eddies that produce the remaining energy transfer from the large to the small scales.

Mathematical and physical constraints of LES have been the subject of several recent studies, including studies of the LES equations and commutation errors,[10,11] the role of discretization errors,[12] and the use of frame indifference[10,13] and realizability.[10,14] From these, B is known to be symmetric, positive definite, and frame indifferent (invariant under arbitrary change of frames) and therefore an isotropic function in its arguments. The realizability conditions follow from the properties of B, and the necessary and sufficient conditions for B being positive definite can be expressed in terms of the principal invariants of B, i.e., $\mathrm{tr}\,B \geq 0$, $k \geq \frac{1}{2}\|B\|$, and $\det B \geq 0$. Most SGS models are known to comply with the first and second of these constraints. However, the last constraint is generally not satisfied,[10] but at present this is not considered a serious drawback, although more theoretical and computational research is required to establish this.

The understanding of L, C, and R is generally deficient, and the uncertainty in the modeling defeats any attempt at precision. However, because energy cascades primarily from the large-scale to the small-scale eddies where it eventually is dissipated by physical viscosity, the main role of models for B is to channel the appropriate amount of energy away from the resolved scales. Differential or algebraic-type models can be used, but so far only a few attempts have been made to use differential-type models because they are expensive and complicated to implement. Algebraic-type models can be derived from B, being an isotropic function in its arguments, which for isochoric flows implies that $B = \alpha_0 I + \alpha_1 \bar{D} + \alpha_2 \bar{D}^2$, where α_i are functions of the principal invariants of $\bar{D}$. The most versatile algebraic models are linear in the deviatoric part of $\bar{D}$ and thus purely dissipative, i.e.,

$$B = \tfrac{2}{3}kI - 2\nu_k\bar{D}_D = \tfrac{1}{3}(2k + \mathrm{div}\,\bar{v})I - 2\nu_k\bar{D} = \tfrac{2}{3}kI - 2\nu_k\bar{D} \quad (2)$$

unambiguously satisfying symmetry and the principle of frame indifference.[15–17] Dimensional arguments suggests that the eddy-viscosity ν_k should be given by the product of a velocity scale υ and a length scale λ; λ is related to Δ, but various models differ in their prescription for υ.

In this investigation four eddy-viscosity models will be used; two eddy-viscosity models use a modeled version of the k equation to model υ. Assuming that the triple correlation can be represented by $\mathrm{div}(\nu_k\,\mathrm{grad}\,k)$ and the SGS dissipation scales as $\varepsilon = \upsilon^3/\lambda$, we have

$$\partial_t(k) + \mathrm{div}(k\bar{v}) = -B \cdot \bar{D} + \mathrm{div}(\nu_k\,\mathrm{grad}\,k) + c_\varepsilon k^{\frac{3}{2}}\Delta^{-1}$$

$$\nu_k = c_k\Delta\sqrt{k} \qquad (3)$$

where $c_k \approx 0.07$ and $c_\varepsilon \approx 1.05$, which constitutes model A1.[18] Kim and Menon[19] and Ghosal et al.[20] have proposed dynamic versions of Eq. (3) because c_k and c_ε should be determined from local information only and to avoid the ad hoc averaging or the additional computational complexity in solving two additional integral equations the former model is selected and referred to as model A2. Thus, $c_k = (L \cdot M)/(M \cdot M)$ and $c_\varepsilon = e/m$, where $L = \overline{\bar{v} \otimes \bar{v}} - \bar{\bar{v}} \otimes \bar{\bar{v}}$, $M = -2\bar{\Delta}(\frac{1}{2}\,\mathrm{tr}\,L)^{1/2}\bar{\bar{D}}$, $e = \nu(\overline{\bar{D} \cdot \bar{D}} - \bar{\bar{D}} \cdot \bar{\bar{D}})$, and $m = \bar{\Delta}^{-1}(\frac{1}{2}\,\mathrm{tr}\,L)^{3/2}$, where the second level of filtering uses an anisotropic finite volume

Table 1 Overview over the different SGS models investigated in the present study

Model	Definition	Features
A1	(2) + (3)	Constant coefficient one-equation eddy-viscosity model
A2	(2) + (3)	Dynamic coefficient one-equation eddy-viscosity model
B1	(2) + (4)	Constant coefficient Smagorinsky eddy-viscosity model
B2	(2) + (4)	Dynamic coefficient Smagorinsky eddy-viscosity model

equivalent of the filter in terms of the Laplace operator. A particular advantage of this model is that $\mathrm{tr}\,L > 0$, thereby avoiding the numerical ill conditioning of most dynamic models. The remaining eddy-viscosity models are of algebraic nature so that k and ν_k follow from equilibrium solutions of Eq. (3), i.e.,

$$k = c_I\Delta^2\|\bar{D}\|, \qquad \nu_k = c_D\Delta^2\|\bar{D}\| \qquad (4)$$

where $c_I \approx 0.13$ and $c_D \approx 0.02$ Ref. 21, which constitutes model B1. Dynamic forms of model B1 have been proposed by Germano et al.[17] and by Ghosal et al.[20]; for model B2 we therefore take $c_I = \langle m_2^{1}\,\mathrm{tr}\,L\rangle/\langle m^2\rangle$ and $c_D = \langle L \cdot M\rangle/\langle M \cdot M\rangle$, where $M = \Delta^2\|\bar{D}\|\bar{D} - \bar{\Delta}^2\|\bar{\bar{D}}\|\bar{\bar{D}}$ and $m = \bar{\Delta}^2\|\bar{\bar{D}}\|^2 - \Delta^2\|\bar{D}\|^2$. The additional averaging or smoothing $\langle \cdot \rangle$ is here performed locally over a region having the radius $2|d|$, where d is the distance between adjacent grid points. A common feature of eddy-viscosity models is that k can be combined with the pressure $\bar{p}$, and thus it is not essential to know k. See Table 1 for a summary of the different SGS turbulence models used.

III. Numerical Methods and Computational Details

The LES equations (1) are discretized using the finite volume method, where the domain D is divided into cells Ω_P so that $\cup_P(\Omega_P) = D \cup \partial D$ and $\cap_P(\Omega_P) = \varnothing$. Letting

$$f_P = \frac{1}{\delta V_P}\int_{\Omega_P} f\,\mathrm{dV}$$

represent the approximation to the cell average of f over the Pth cell, Gauss theorem can be used to derive the semidiscretized LES equations. Following Rhie and Chow,[22] $\mathrm{grad}\,\bar{p}$ is not discretized at this stage, and the discretized momentum equation is integrated in time using a multistep method[23]:

$$\sum_f (\bar{v} \cdot \mathrm{d}A)_f = 0$$

$$\sum_{k=1}^{m}\left\{\alpha_k(\bar{v})_P^{n+k} + \frac{\beta_i\Delta t}{\delta V_P}\sum_f [(\bar{v} \cdot \mathrm{d}A)\bar{v} - (\bar{S} - B)\,\mathrm{d}A]_f^{n+k}\right\}$$

$$= -\beta_i\left[(\mathrm{grad}\,\bar{p})_P^{n+k} + f\right]\Delta t \qquad (5)$$

where α_k and β_k are parameters of the scheme and Δt the time step. Here, let $\tilde{f}_f^C(\bar{v}; \mu)$ represent an approximation to the convective flux $f_f^C(\bar{v}) = [(\bar{v} \cdot \mathrm{d}A)\bar{v}]_f = F_f\bar{v}_f$ and $\tilde{f}_f^D(\bar{v}; \mu)$ an approximation to the combined viscous and SGS flux $f_f^D(\bar{v}) = [(S - B)n]_f$, where $\mu = \mu(P)$ represent a set of grid points in the neighborhood of P. The functional reconstruction of $\tilde{f}_f^C(\bar{v}; \mu)$ and $\tilde{f}_f^D(\bar{v}; \mu)$ is carried out using linear interpolation across all cell faces f of Ω_P and centered difference approximations of the inner gradients in $\tilde{f}_f^D(\bar{v}; \mu)$, resulting in centered second-order accurate representations of the convective and combined fluxes, respectively. Time integration is performed by the Crank–Nicholson scheme, $m = 1$, $\alpha_0 = -\alpha_1 = 1$, $\beta_0 = \beta_1 = \frac{1}{2}$, and $\alpha_2 = \beta_2 = 0$. To decouple the pressure-velocity system, the second equation of Eq. (5) is solved for $\bar{v}_P^{n+m}$, the face interpolate of which is used to derive the flux F_f. Eliminating $\bar{v}_f^{n+m}$ between the first equation of Eq. (5) and the derived expression for $\bar{v}_P^{n+m}$ then results in the discrete Poisson equation

Table 2   Global parameters for LES of the flow around a square prism in a rectilinear channel ($Sr = fh/v_0$ is the Strouhal number, where f is the frequency of the vortex shedding, λ is the length of the time-averaged separation region behind the prism, $\langle c_D \rangle$ is the time-averaged drag coefficient, and c'_D and c'_L are the fluctuating drag and lift coefficients, respectively).

Simulation model	Grid	Block	$\langle v'_1/v_0 \rangle$	Width	λ/h	Sr	$\langle c_D \rangle$	c'_D	c'_L
LES: Model A1	$10{,}800 \times 24$, A	0.07	——	$4h$	1.23	0.129	2.2	0.19	1.32
LES: Model A2	$10{,}800 \times 24$, A	0.07	——	$4h$	1.24	0.130	2.1	0.18	1.32
LES: Model B1	$10{,}800 \times 24$, A	0.07	——	$4h$	1.31	0.134	2.0	0.17	1.29
LES: Model B2	$10{,}800 \times 24$, A	0.07	——	$4h$	1.33	0.132	2.0	0.20	1.34
LES: Model B1	$10{,}800 \times 48$, B	0.07	——	$8h$	1.25	0.131	2.1	0.17	1.30
LES: Model A1	$14{,}600 \times 24$, C	0.07	——	$4h$	1.37	0.135	2.1	0.19	1.34
RAS: k-ε (Ref. 4)	$10{,}800$, D	0.07	——	——	2.45	0.112	1.65	0.03	0.31
RAS: LRR[29]	$10{,}800$, D	0.07	——	——	1.32	0.124	1.8	0.15	1.17
Exp.,[24] $Re = 2.14 \times 10^4$	——	0.07	0.02	$9.75h$	1.38	0.132	2.05	——	——
Exp.,[25] $Re = 1.4 \times 10^4$	——	0.13	0.06	——	1.32	0.139	——	——	——

$$\sum_f \left\{ \left(a_P^{-1}\right)_f \left[\mathrm{grad}(\bar p)_f^{n+m} \cdot \mathrm{d}\boldsymbol{A}\right] \right\} = \sum_f \left\{ \left(a_P^{-1}\right)_f \left[\sum_{i=0}^{m} \sum_N \left(a_N^{n+i} \bar v_N^{n+i}\right) \right. \right.$$

$$\left. \left. + \sum_{i=0}^{m-1} \left(b_P^{n+i} \bar v_P^{n+i}\right) \right]_f \cdot \mathrm{d}\boldsymbol{A} \right\} \tag{6}$$

Equations (5) and (6) are solved sequentially with iteration over the explicit coupling terms to obtain convergence. The implicit method used results in a Courant number restriction; it is found that a maximum Courant number of 0.5 gives satisfactory numerical stability and temporal accuracy, but a value of 0.2 is preferable for temporal accuracy. When the SGS model is based on Eq. (3), the discretized balance equation for k is solved before the other equations.

The accuracy of the numerical scheme employed when solving Eq. (1) is of particular importance in LES because div $\boldsymbol{B}$ is formally of order $\mathcal{O}(\Delta^{n-1})$. The numerical scheme should thus have a leading-order truncation error of $\mathcal{O}(\Delta^n)$ or higher to avoid interaction with the SGS models. The truncation error $\mathcal{F}$ can be derived from the modified equation approach, involving Taylor-series expansion of the finite volume versions of the LES equations. For the LES momentum equation (5),

$$\mathcal{F} = \tfrac{1}{3}(\Delta t)^2 \delta_t^3(\bar v) + \mathrm{div}\left[\left(\tfrac{1}{6}\bar v \otimes \boldsymbol{d} \otimes \boldsymbol{d}\right)(\mathrm{grad}(\mathrm{grad})\, \bar v)\right]$$

$$+ \mathrm{div}\left(\left(\nu \tfrac{1}{12}\boldsymbol{d} \otimes \boldsymbol{d}\right)\{\mathrm{grad}[\mathrm{div}(\mathrm{grad}\, \bar v)]\}\right) \tag{7}$$

The leading-order truncation error is of $\mathcal{O}(\Delta t^2, |\boldsymbol{d}|^2)$, and for small Courant numbers (typical of LES and DNS) the transient contribution can be neglected; this indicates that second-order dispersion and third-order dissipation dominates together with the explicit SGS model.

IV.   Description of the Flow Problem and the Simulations

The flow configuration is presented in Fig. 1a and has a cross section of $10\,h \times 14\,h$ and a length of $20.5\,h$, where h is the height of the prism. The bulk Reynolds number, based on h and the inlet velocity v_0, is 2.14×10^4. Experimental results are available from different sources; Lyn et al.[24] present ensemble-averaged and phase-averaged velocity components, rms-velocity fluctuations, and the turbulent shear stress at $x_1/h = 1, 2, 8$ and at the centerline $x_2/h = 0$ for $Re = 2.14 \times 10^4$; Durao et al.[25] give ensemble-averaged velocity components, the rms-velocity fluctuations, and the turbulent shear stress at $x_1/h = 1, 2$ and at the centerline $x_2/h = 0$ for $Re = 1.48 \times 10^4$. As the experimental data are nondimensionalized with h and v_0, the statistical moments of the velocity from Refs. 24 and 25 are expected to collapse onto one line. However, this is found not to be the case for the streamwise centerline velocity. A comprehensive summary of the simulations is given in Table 2 together with a selection of local time-averaged global parameters.

All simulations start from rest, and the unsteady flow characteristics evolve naturally. At the inlet $\bar v = v_0 \boldsymbol{e}_1 + \boldsymbol{u}'$, where $\boldsymbol{e}_k$ is a unit vector in the x_k direction and $\boldsymbol{u}'$ represents a random perturbation of the order of 2% of v_0 that emulates the upstream turbulence
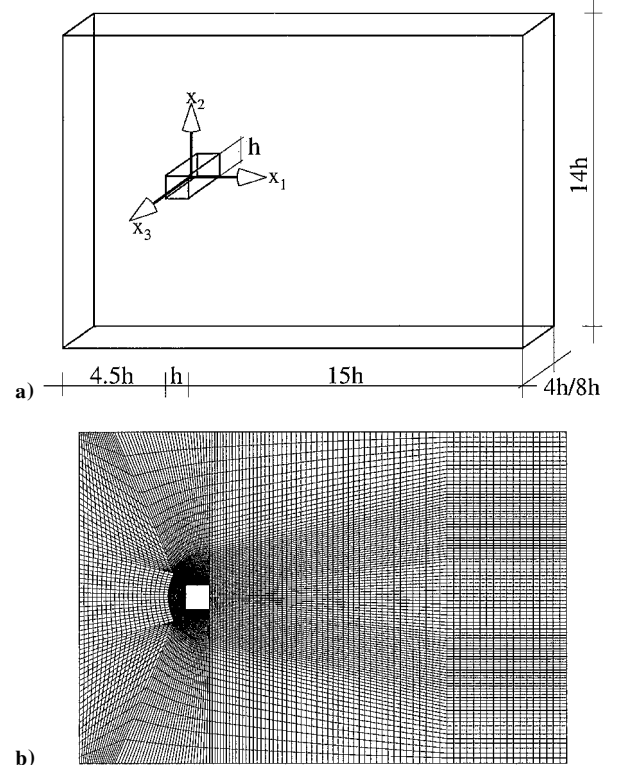
Fig. 1   Schematic of a) the computational domain and b) the grid.

and grad $\bar p \cdot \boldsymbol{e}_1 = 0$. No noticeable effects were found on the statistics of $\bar v$ or on the flow topology when changing the magnitude of $\boldsymbol{u}'$ as the large-scale structures absorb the fluctuations artificially imposed at the inlet.[26] At the outlet $\bar p = p_0$, while $\bar v$ is subjected to a zero Neumann condition. The channel width and the spatial resolution influence the attributes of the flow and the statistical moments of $\bar v$.[27] Available computer resources oblige us to find a compromise between ample spanwise extent and sufficient resolution. In this study two spanwise extents have been used: $4h$, which is the standard width, and $8h$. To minimize contamination from two-dimensional structures, a semiartificial free-slip condition [$\bar v_3 = 0$ and $(\mathrm{grad}\, \bar v)_{kk} = 0$, $k = 1, 2$] is applied on the planes $x_3 = \pm 2h$ and $\pm 4h$. In the corresponding laboratory experiment the upper and lower boundaries $x_2 = \pm 7h$ are walls. Here, we assume that the effects of the these boundaries on the development and maintenance of the coherent structures can be neglected and slip conditions be applied. The prism boundary condition poses a serious problem; guided by results from channel flow simulations,[28] $\bar v = \boldsymbol{0}$ is adopted, although this requires a fine grid around the prism. Nonuniform Cartesian grids support only hexahedral cells aligned with the flow domain, resulting in grids with large aspect ratios or a topology that does not follow the mean flow or an excessive number of cells. To avoid these problems, a C-shaped grid of hexahedral cells swept around the prism is used. This type of grid allows us to optimize the

spatial resolution around the prism and to avoid the excessive aspect ratios typical of standard nonuniform Cartesian grids. The flow around the prism is temporally and spatially complex, including interactions between separated shear layers and regions of irrotational flow entering the wake. This, together with the no-slip condition, requires high resolution; this can be achieved by using local grid refinement as examined in simulations performed on grid D (see also Table 2).

For comparison we include results from two time-dependent RAS models in this study: the standard k-ε model[4] and the differential stress equation model of Launder et al. (the LRR model).[29] The RAS models are discretized by the same numerical methods as used for the LES models and use two-dimensional versions of the LES grid. Inlet values of k and ε are selected to match those of the experimental data, i.e., the turbulence intensity is set to 2% of v_0 and the dissipation is given by the relation $\varepsilon_{\text{inlet}} = c_\mu^{3/4} k^{3/2} / 0.07 h$, where h is the height of the prism. Wall functions that relate the wall shear stress, the tangential velocity at the first cell of the wall, production of k and dissipation ε by means of the logaritmic law of the wall were used; furthermore, $n^+ \approx 10$ for the first set of grid points so that their centers lies within the log-law region.

V.   Statistics of Global Flow Parameters

Table 2 summarizes different global parameters such as the dimensionless shedding frequency or the Strouhal number $Sr = f h / v_0$, calculated from the time history of $\bar{v}$ in a set of descrete points, the time-averaged or mean drag coefficient $\langle c_D \rangle$, the rms values of the fluctuations of the drag and lift coefficients c_D' and c_L', and the recirculation length λ. We adopt the relations suggested in Ref. 28, i.e., $\langle c_D \rangle = 2 F_D / (A \rho v_0^2)$ and $\langle c_L \rangle = 2 F_L / (A \rho v_0^2)$, respectively, where F_D and F_L are the drag and lift forces (including both viscous and pressure contributions), ρ the density, and A is the frontal area of the prism. For the rms fluctuations, $c_D' = \sqrt{\langle (c_D - \langle c_D \rangle)^2 \rangle}$ and $c_L' = \sqrt{\langle (c_L - \langle c_L \rangle)^2 \rangle}$ are used. The recirculation length λ is defined as the distance downstream of the prism after which the streamwise velocity fluctuations have reached a maximum, hence defining the length of the mean separation region behind the prism. Strouhal numbers resulting from LES are in good agreement with the data from Ref. 24 and in marginal agreement with the data from Ref. 25. This is believed to be related to the difference in blockage between the configurations; for the Ref. 25 case the blockage is 13%, whereas for the Ref. 24 case, and in the simulations, the blockage is 7%. Moreover, the Strouhal number seems insensitive to the choice of SGS models. In contrast, the Strouhal numbers resulting from the RAS models are underpredicted. For LES the mean drag coefficient $\langle c_D \rangle$ is also in good agreement with the experimental data irrespective of the SGS model; all LES models give values of $\langle c_D \rangle$ within the parameter range given by the data. In contrast, most RAS models predict $\langle c_D \rangle$ too low as a result of a disproportionate base pressure and associated with a long separation region. The recirculation length shows variations representative of the different LES models and the different grids used. On the reference grid (i.e., grid A), model A2 gives the best prediction of λ, followed by models A1, B1, and B2; on grid B there is virtually no improvement, but on the refined grid (grid C) a notable improvement is found. This suggests that grid A is too coarse to resolve the important structures in the formation and recovery regions. The rms fluctuations of c_D and c_L show minor variations with the SGS model, whereas most RAS models results show noticeably smaller values of c_D' and c_L'.

## VI.   Comparison of First- and Second-Order Statistical Moments

In Fig. 2 the first-order statistical moments of the resolvable velocity $\langle \bar{v} \rangle$, nondimensionalized by the inlet velocity v_0, are shown at the cross sections $x_1 / h = 1$, 2, and 8 and at the centerline $x_2 / h = 7$. The first cross section lies within the recirculation region, defined by $x_1 / h < \lambda / h \approx 1.37$. The second cross section is in the recovery region, i.e., between the closure point of the recirculation zone λ / h and $x_1 / h < 4.7$, where the flow accelerates despite the adverse pressure gradient. The third cross section is in the near-wake region, i.e.,

within $4.7 < x_1 / h < 10$. Profiles from all LES models, the experimental data of Refs. 24 and 25, and the results from the k-ε model are presented. The uncertainty in the data from Ref. 24 is estimated to be less than 5%, with the largest uncertainty in $\langle \bar{v}_2 \rangle$. Good agreement between the experimental results prevails in the recirculation region $x_1 / h < \lambda / h$ and in the upstream part of the recovery region $\lambda / h < x_1 / h < 2.3$, whereas in the downstream part of the recovery region $2.3 < x_1 / h < 4.7$ and in the entire wake region $x_1 / h > 4.7$, differences are found. The suggestion has been made[24] that these differences may be attributed to differences in experimental conditions, such as the higher inlet turbulence level, larger blockage, or smaller aspect ratios of the case in Ref. 25. Specifically, the effect of the larger blockage in the Ref. 25 case is evident from the profile of $\langle \bar{v}_1 \rangle / v_0$ at $x_1 / h = 1$, which approaches 1.4 instead of 1.2 as for the Ref. 24 case.

The streamwise velocity profiles across the wake (Figs. 2a–2c) and the centerline profile (Fig. 2d) suggest that LES, irrespective of the SGS model, offers more accurate predictions than the RAS models tested. In particular, the longer recirculation region in the RAS induces a downstream shift of the entire streamwise velocity distribution on the centerline. This shift is apparent not only on the centerline but also in profiles at $x_1 / h = 1$ and 2, where the wake is wider and the velocity deficit is larger in the RAS than in any of the LES models. In general, the LES results appear virtually independent of the SGS model; comparing LES performed on grid A, only small differences can be detected. Models A1 and A2 not only predict the length of the recirculation region better than models B1 and B2 (see Table 1), but also the one-equation models are superior in reproducing the velocity profiles in the recirculation region. At present, this is ascribed to hereditary and nonequilibrium effects catered for only by models A1 and A2. However, none of the LES managed to reproduce the high negative streamwise velocity in the recirculation zone. A possible source of error could be that the spanwise extent of the domain is insufficient. However, attempts to widen the domain from $4h$ to $8h$ in the spanwise direction (grid B) did not show any improvements. Local grid refinement in regions around the prism and in the recovery region ($-0.5 < x_1 / h < 5$ and $-2 < x_2 / h < 2$) proved successful (i.e., grid C), and LES performed on this grid show good agreement with data both in the recirculation region and in the early part of the recovery region. Farther downstream the results from all simulations approach the freestream velocity or the data from Ref. 25.

Figures 2e and 2f present the vertical velocity profiles. The peak vertical velocity and its location and downstream shift are correctly captured by all LES models although some differences between predictions, using different SGS models and grids, are evident. The best agreement with the Ref. 24 data is obtained with model A1 on grid C for which the magnitude of $\langle \bar{v}_2 \rangle$ is underpredicted by about 2%. On grid A the best agreement between Ref. 24 and the LES results is obtained with model A2, followed by models A1, B1, and B2. On grid A all LES models underpredict the peak vertical velocity by about 5%. The spanwise extent of the computational domain appears not to influence the distribution of $\langle \bar{v}_2 \rangle$ across the wake. Note, however, that $\langle \bar{v}_2 \rangle$ in the Ref. 25 data at $x_2 / h = 0$ does not approach zero as required by continuity and symmetry. Results from all but the LRR RAS models show that the vertical velocity is underpredicted in the vortex formation region; this leads to incorrect predictions of the convection term in the momentum equation, which has further consequences on the transport of Reynolds stresses. Hence, a full differential stress equation model, like the LRR model, is required to remove this deficiency of RAS models.

Given the velocity fluctuations $\bar{v}' = \bar{v} - \langle \bar{v} \rangle$, the resolvable Reynolds stress tensor is $\boldsymbol{T} = \langle \bar{v}' \otimes \bar{v}' \rangle$ from which the rms-velocity fluctuations become $\bar{v}^{\text{rms}} = \text{diag}(\boldsymbol{T}^{1/2})$. Figures 3a, 3b, and 3e show the streamwise rms-velocity fluctuations $\bar{v}_1^{\text{rms}}$. Following Ref. 24, the uncertainty in the Lyn et al. rms-velocity fluctuations is estimated to be 5%. In the recirculation region, represented by the section $x_1 / h = 1$, the peak values of $\bar{v}_1^{\text{rms}}$ are overpredicted by between 5 and 8% by models B1 and B2 on grids A and B. The opposite holds for models A1 and A2, where the peak values of $\bar{v}_1^{\text{rms}}$ are underpredicted by about 5% on both grids A and C. In the recovery region, represented by the section $x_1 / h = 2$, similar conclusions can be drawn; the different LES models behave similarly, although the
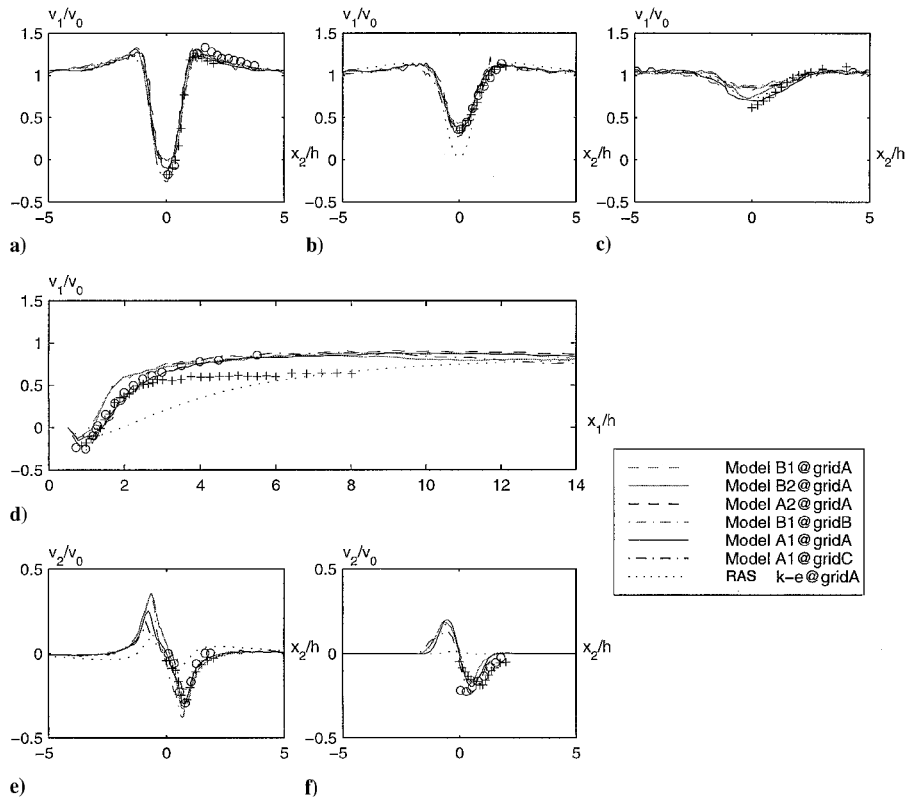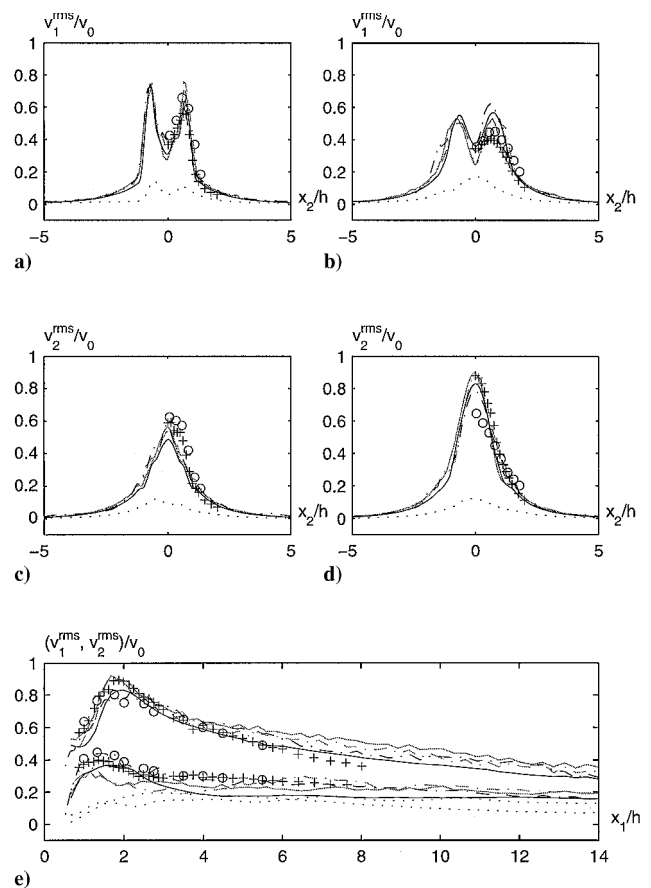
Fig. 2   Profiles of the first-order statistical moments of v nondimensionalized by the inlet velocity v_0 and the prism height h at $x_1/h = 1, 2$, and 8 and at $x_3/h = 0$.

correlation with the experimental data of Ref. 24 is slightly lower. In both cross sections the agreement with the Ref. 25 data is superior because the streamwise rms-velocity fluctuations measured by Durao et al. overshoots the Ref. 24 data by 2–5%, the latter value being in the recovery region. All LES models can accurately reproduce the relative locations of the peak streamwise rms fluctuations and the overall shape of the profiles both across the wake and along the wake centerline.

In Figs. 3c–3e the vertical rms-velocity fluctuations $\bar{v}_2^{rms}$ are presented. In the recirculation region the agreement between the profiles from the individual LES models and the two experimental results is excellent; the simulated profiles are well within the uncertainty interval of 5%. Here the differences between the LES models are less apparent; model A1 on grid C and model B1 on grid A give the best correlation with the Lyn et al. data.[24] The other LES models are virtually inseparable and underpredict the vertical rms-velocity fluctuations by about 5%. The Ref. 25 data show a wider and less peaked profile across the wake. In the recovery region it is evident that the two data sets diverge, forming upper (Ref. 24) and lower (Ref. 25) bounds for the vertical rms-velocity fluctuations in which the results from the LES models can be found. Finally, it is interesting that these results are all biased toward the data of Ref. 24. It is difficult to arrange the LES models in order of precedence, but it seems that models B1 and B2 on grids A and B give the best correlation with the Ref. 24 data closely followed by models A1 and A2 on grids A and C. Thus, the grid seems to play a less vital role in establishing the correct rms-velocity fluctuations compared to establishing the correct first-order statistical moments of the velocity.

In Figs. 4a and 4b the resolvable Reynolds shear stresses T_{12} are presented. In the recirculation region these profiles exhibit two extrema: a minimum as might be expected in the shear-layer regions (located around the global extremum of T_{12}) and an additional local maximum (of opposite sign) nearer to the centerline. Only the data from Ref. 24 support these findings; the data from Ref. 25 show only a maximum in the shear-layer region, which is marginally translated toward the centerline. All LES models reproduce this characteristic feature very well; the differences between the LES results and

Fig. 3   Profiles of the second-order statistical moments $\bar{v}_1^{rms}$ and $\bar{v}_2^{rms}$ nondimensionalized by the inlet velocity v_0 at the locations $x_1/h = 1, 2$, and 8 and $x_2/h = 7$. Legend as in Fig. 2.
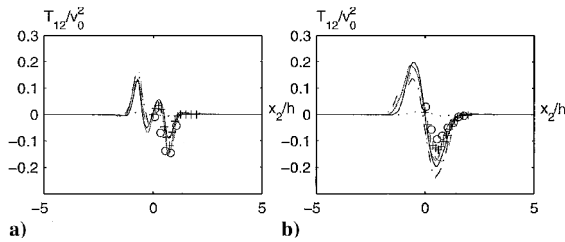
Fig. 4 Profiles of the second-order statistical moment T_{12} nondimensionalized by the inlet velocity v_0 at the locations $x_1/h = 1, 2,$ and 8 and at the centerline $x_2/h = 7$. Legend as in Fig. 2.

the data from Ref. 24 are below the estimated uncertainty levels of 15–25% (cf. Ref. 24) suggested for the experimental results. Differences between the LES results are small and cannot be used to place the SGS models in order of precedence. Simulations performed on the reference grid seem to overpredict T_{12}, whereas simulations performed on the refined grid seem to underpredict T_{12}. In the recovery region the profiles of T_{12} exhibit only one minima defining the position of the shear-layer region. All LES models seem to overpredict the maximum shear stress on the reference grid by approximately 15%; on the refined grid this is reduced to about 10%—in both cases well below the uncertainty level of T_{12}. Because $(\mathrm{grad}\,\bar{v})e_2$ does not change sign at any of the global extrema of T_{12} in the recirculation region, any gradient-transport model in RAS relating $\langle v' \otimes v' \rangle$ to $\mathrm{grad}\langle v \rangle$ will fail. The fact that the local extremum of T_{12} is located closer to the centerline indicates the potential role of transport effects in determining $\langle v' \otimes v' \rangle$. A closer examination of T_{12} using the triple decomposition shows that the second local extrema is caused entirely by the periodic component of T_{12}. None of the RAS models were successful in identifying the second local extrema; this indicates that LES, irrespective of the SGS model, is a better simulation tool.

VII. Analysis of Phase-Averaged Flow Structures

To advance our understanding of the coherent structures, one simulation (model A1 on grid C) was run for five additional shedding cycles. Data were collected 20 times per shedding cycle and averaged to generate ensemble-averaged data at constant phases during the shedding cycle. Extending the number of cycles would improve statistics but was impractical given the constraints of computational resources. These data were compared with experimental results of Lyn et al.[24] by examining the shedding at the midpoint of the top prism wall. Following Reynolds and Hussain,[30] the triple decomposition $v = \langle v \rangle + \tilde{v} + v'$, where $\tilde{v} = [v] - \langle v \rangle$ is the periodic mean and $[v]$ is the mean at constant phase, now becomes $v = [v] + v'$. Hence, $[v'] = 0$, $[\tilde{v}] = 0$, and $[\tilde{v} \otimes v'] = 0$. The continuity and momentum equations for the mean flow at constant phase and the global mean flow are

$$\mathrm{div}[v] = 0$$

$$\partial_t[v] + \mathrm{div}([v] \otimes [v]) = -\mathrm{grad}[p] + \mathrm{div}(v\,\mathrm{grad}[v]) - \mathrm{div}[v' \otimes v']$$

and

$$\mathrm{div}\langle v \rangle = 0$$

$$\mathrm{div}(\langle v \rangle \otimes \langle v \rangle) = -\mathrm{grad}\langle p \rangle + \mathrm{div}(v\,\mathrm{grad}\langle v \rangle) - \mathrm{div}\langle [v' \otimes v'] \rangle$$
$$- \mathrm{div}\langle \tilde{v} \otimes \tilde{v} \rangle \qquad (8)$$

The momentum equation in the first equation of Eq. (8) includes only the conventional Reynolds-stress tensor generated by spatially local fluctuations at constant phase. It controls the dynamics of the coherent structures and operates at a lower level than the analogous stresses in the second equation of Eq. (8). Hence, turbulence can be interpreted as a local phenomenon attached to and moving with the vortices and their saddle points. For RAS turbulence modeling it is important to examine $\langle \tilde{v} \otimes \tilde{v} \rangle$ and $[v' \otimes v']$ so the relative contributions of the periodic and random motions to the Reynolds stress in the second equation of Eq. (8) can be understood.

Figure 5 shows the velocity in the plane $-1 < x_1/h < 10$, $|x_2/h| < 3$, and $x_3/h = 2$ in a frame of reference fixed with respect
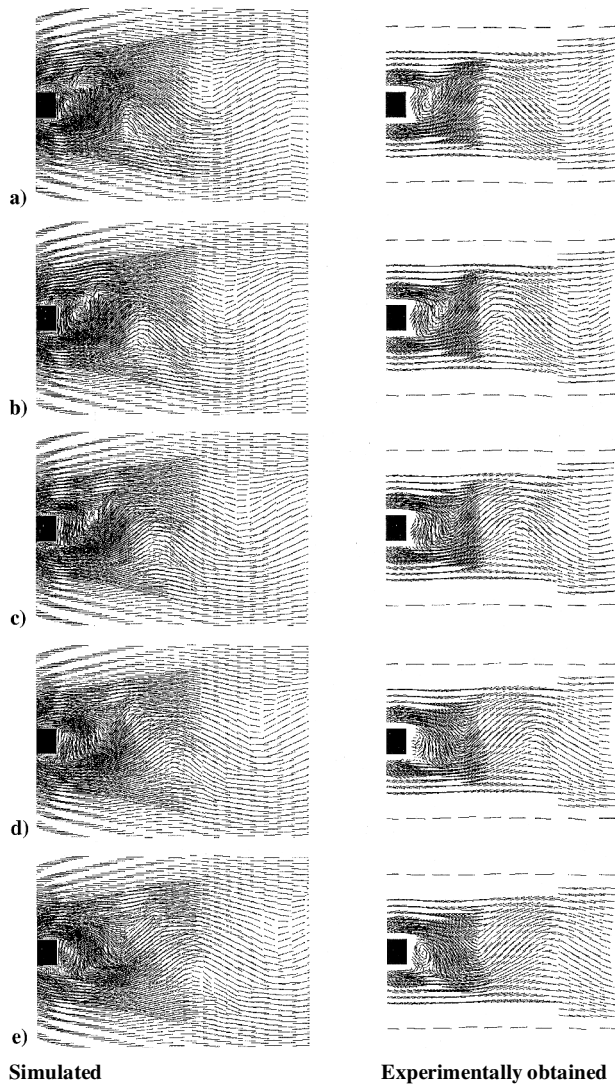
Fig. 5 Velocity field at constant phase as viewed from a frame of reference fixed with respect to the prism. These are five evenly spaced realizations covering half of a representative shedding cycle (the other half being symmetrical).

to the prism at five phases during one-half of the shedding cycle from LES (left column) and from the experimental data (right column). The other half of the cycle repeats the data in these figures after reflection in $x_2/h = 0$. Reasonable agreement between LES and experimental data is found; in particular the phase variation of $\bar{v}$ from LES matches the phase variation in the experimental data, supporting the conjecture that phase information is retained at the large scales of the flow and is thus available from LES. Vortices traverse the sides of the prism to be shed off the downstream corners to interact and merge with other vortical structures. In the experimental data only the strongest vortices are seen, and far downstream they merge into a wavy structure, but their centers and saddles correlate well with those of the LES results. An important kinematic feature associated with entrainment of ambient fluid by the shedding vortices is the formation and evolution of a saddle point. Evidence of this begins to appear in Fig. 5a where the saddle starts to develop, so that by Fig. 5e it is fully developed. The converging separatrix of the saddle brings in ambient fluid from above and below the prism, while the diverging separatrix carries fluid downstream into a strong vortex where a process of fluid roll up is occurring.

To examine the flow, we may also study the evolution of the mean vorticity at constant phase, i.e., $[\tilde{\omega}] = \frac{1}{2}\mathrm{curl}[\bar{v}]$. Figure 6 shows the spanwise component, i.e., $[\tilde{\omega}]_3$, at phase 4 from LES (Fig. 6a) and from experiments (Fig. 6b). After the vortices are shed of the prism, they move for some distance essentially parallel with and close to the centerline, with the centroids of vorticity lying approximately
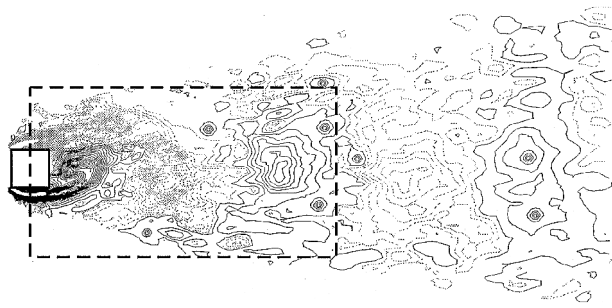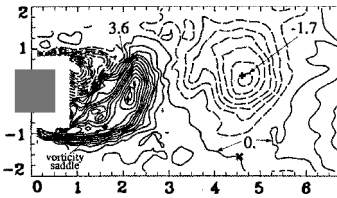
a) Simulated

b) Experiments[24]

Fig. 6   Spanwise vorticity $[\tilde{\omega}]_3$ at phase 4 as observed from a frame of reference fixed with respect to the prism. Gray contour lines denote negative values, and black denotes positve values. The vorticity span is $-11.3 < [\tilde{\omega}]_3 h/v_0 < 12.3$.

$3.2h$ apart, but less than $0.5h$ from the wake centerline. Thus, the geometric configuration of the vortex street is somewhat different from the equilibrium configuration first proposed by von Kármán.[31] The agreement with the experimental data is reasonably good supporting the assertion that LES can be used in analyzing unsteady flow wake flow. The peak values of $[\tilde{\omega}]_3$ obtained from simulations (model A1 on grid C) and experiments agree to within 10%.

The reason for ensemble averaging at constant phase is that an important fraction of the flow is periodic in time. In the context of RAS, these fluctuations include contributions from the periodic large-scale motion and the small-scale turbulence. From the point of view of the global mean flow, described by the first equation in Eq. (8), the Reynolds stresses are associated with both periodic and turbulent motions, of which the former is resolved by LES, whereas the latter is generally not resolved by LES. In Fig. 7 the periodic stress components $(\tilde{v} \otimes \tilde{v})_{11}$, $(\tilde{v} \otimes \tilde{v})_{22}$, $(\tilde{v} \otimes \tilde{v})_{33}$, and $(\tilde{v} \otimes \tilde{v})_{12}$ are presented at phase 4. Superposition of these on each other and on the vorticity (Fig. 6a) suggest that the range of periodic stresses extends outside the turbulent portion of the wake. The stress pattern also shows some symmetry with respect to the wake centerline. The motion is essentially a local rotation (with respect to the global mean) generating peaks in $(\tilde{v} \otimes \tilde{v})_{11}$ above and below each vortex with $\tilde{v}_1$ positive for one peak and negative for the other. Similarly, alternating peaks in $(\tilde{v} \otimes \tilde{v})_{22}$ conform with positive and negative peaks in $\tilde{v}_2$. The peaks in $(\tilde{v} \otimes \tilde{v})_{33}$ coincide with the $\tilde{\omega}_3$ vortices, suggesting momentum entrainment in the x_3 direction through the $\tilde{\omega}_3$ vortices. The shear stress $(\tilde{v} \otimes \tilde{v})_{12}$ is antisymmetric about the centerline, and regions of intense momentum flux toward the centerline are separated by regions of weak momentum flux away from the centerline. The intrusion of ambient fluid into the braid region between the $\tilde{\omega}_3$ vortices thus results in large shear stresses.[32]

Figure 8 shows the turbulent stress components $[\tilde{v}' \otimes \tilde{v}']_{11}$, $[\tilde{v}' \otimes \tilde{v}']_{22}$, $[\tilde{v}' \otimes \tilde{v}']_{33}$, and $[\tilde{v}' \otimes \tilde{v}']_{12}$ at phase 4. For the normal stress components a series of maxima corresponding to the vortex centers with connecting ridges between them is found; the range of these stress structures extends well outside the wake. The stresses caused by the turbulent motion appear to be larger but of the same size as the stresses generated by the large-scale periodic motions, implying that a considerable fraction of the unresolved momentum transport in Eqs. (8) takes place through the turbulent fraction of the flow. This may help to identify why ordinary RAS turbulence models often fail when applied to unsteady wake flow (cf. Figs. 2–4). The
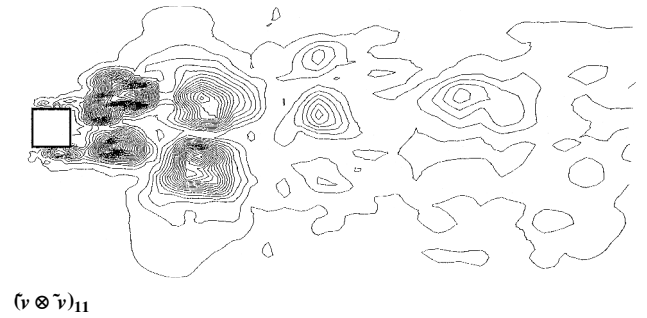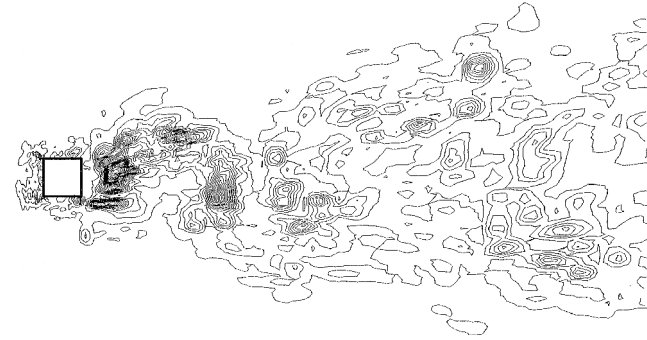

$(v \otimes \tilde{v})_{11}$

$(v \otimes \tilde{v})_{22}$

$(v \otimes \tilde{v})_{33}$

$(v \otimes \tilde{v})_{12}$

Fig. 7   Periodic Reynolds-stress components at phase 4 as observed from a frame of reference fixed with respect to the prism. Gray contour lines denote negative values, and black denotes positive values.

contribution to the shear stress by the turbulent motion $[\tilde{v}' \otimes \tilde{v}]_{12}$ is found to have a peak at the saddle point between the vortices; this behavior is in sharp contrast to the observed behavior of the normal stress components.

The production of turbulent kinetic energy at constant phase $[p] = -[\tilde{v}' \otimes v'] \cdot \text{grad}[v]$ plays the role of an energy sink for the mean flow and an energy source for the turbulent fluctuations. In Fig. 9 $[k] = \frac{1}{2}[v]^2$ and $[p]$ are presented at phase 4. Hence, peaks in $[p]$ lie close to both saddle points and shear-stress extrema. Turbulence seems to be produced mainly in the braids between the large vortices and then advected to and accumulated in the vortices. Because the peaks in production are close to the saddles, being regions of high strain and stretching, the assumption can be made that production of turbulence occurs mainly by stretching vorticity elements oriented along the diverging separatrices, which cross at right angles in the absence of local mean vorticity. Given that
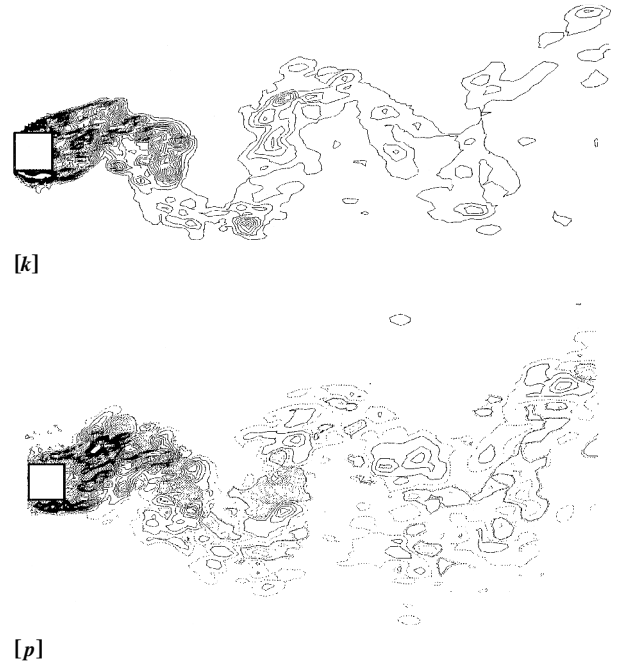
$[\bar{v}' \otimes \bar{v}']_{11}$

$[\bar{v}' \otimes \bar{v}']_{22}$

$[\bar{v}' \otimes \bar{v}']_{33}$

$[\bar{v}' \otimes \bar{v}']_{12}$
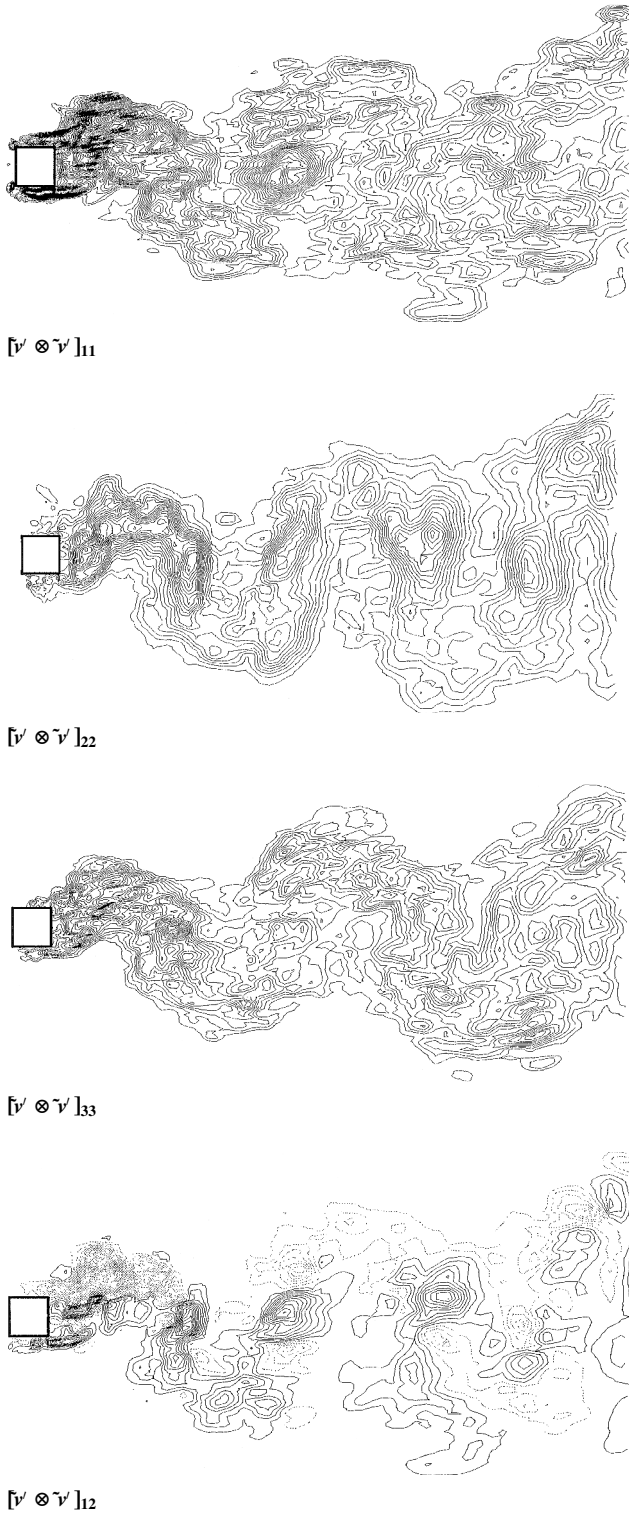
Fig. 8 Turbulent Reynolds stresses at phase 4 as observed from a frame of reference fixed with respect to the prism. Gray contour lines denote negative values, and black denotes positive values.

$[k]$

$[p]$

Fig. 9 Turbulent kinetic energy at constant phase $[k] = \frac{1}{2}[v]^2$ and production of turbulent kinetic energy at constant phase $[p] = -[v' \otimes v'] \cdot \mathrm{grad}[v]$ at phase 4 as viewed from a frame of reference fixed with respect to the prism: Gray contour lines denote negative values, and black denotes positive values.

turbulence is already present near the saddles, this turbulence is continuously amplified to maintain a state of equilibrium. If the entrainment velocity were not maintained at a sufficiently high value, the flow would break up into islands of turbulence near each center that would presumably decay. Turbulence is thus strongly coupled to the strain associated with the nonsteady mean velocity field.

VIII. Analysis of Instantaneous Resolvable Flow Structures

To gain further insight into the dynamics of the coherent structures and the effects of the SGS models on the dynamics, we compare

visualizations of the resolvable vorticity $\bar{\omega}$ from models A1 and A2 on grid A. The resolvable vorticity $\bar{\omega} = \frac{1}{2}\,\mathrm{curl}\,\bar{v}$ satisfies the Helmholtz equation:

$$\partial_t(\bar{\omega}) + \mathrm{div}(\bar{\omega} \otimes \bar{v}) = \mathrm{div}(\nu\,\mathrm{grad}\,\bar{\omega}) + (\mathrm{grad}\,\bar{v})\bar{\omega}$$
$$- \tfrac{1}{2}\,\mathrm{curl}(\mathrm{div}\,\boldsymbol{B}_D) + \tfrac{1}{2}\,\mathrm{curl}\,\bar{f} \qquad (9)$$

where $(\mathrm{grad}\,\bar{v})\bar{\omega}$ describes the stretching of $\bar{\omega}$ by $\bar{v}$ and $\frac{1}{2}\,\mathrm{curl}(\mathrm{div}\,\boldsymbol{B}_D)$ represents the effects of the SGS model on the distribution of $\bar{\omega}$. Figure 10a shows a perspective view of the flow around and behind the prism in terms of iso-surfaces of the spanwise $\bar{\omega}_3$ and longitudinal $\bar{\omega}_{12} = \sqrt{(\bar{\omega}_1^2 + \bar{\omega}_2^2)}$ vorticity components at $v_0/4h$ and $v_0/2h$, respectively. The three-dimensional vortex structures and the detached shear layers at the top and bottom walls of the prism are clearly visible, although the complexity of the structures, and thus the iso-surfaces, obscures the interpretation. However, from Fig. 10a we conclude that the vortical structures consist mainly of spanwise quasi-two-dimensional $\bar{\omega}_3$ vortices interspersed with secondary longitudinal $\bar{\omega}_{12}$ vortices. The $4h$ spanwise extent of the computational domain contains four pairs of counter-rotating longitudinal vortices. The finding that there is about one pair of counter-rotating longitudinal vortices per prism height is further supported by the results obtained using model B1 on grid B, where eight pairs of counter-rotating longitudinal vortices were found. To facilitate the qualitative discussion of the vorticity and the following comparison of $\bar{\omega}$ between different LES results, the three-dimensional visualization of Fig. 10a is complemented by iso-lines of the spanwise vorticity $\bar{\omega}_3$ in the vertical plane $x_3/h = 0$ (Fig. 10b), the longitudinal vorticity $\bar{\omega}_{12}$ in the cross sections $x_1/h = 2$ and 8 (Figs. 10c and 10d, respectively), and in the horizontal plane $x_2/h = 0$ (Fig. 10e). A more complete qualitative discussion can thus be presented: Whenever vortex lines are deformed by the flow, e.g., by the corners of the prism, the presence of shear will create $\bar{\omega}_3$ vortices through Kelvin–Helmholtz instabilities in the shear layers originating at the separation points at the upstream corners of the prism. Furthermore, the $\bar{\omega}_3$ vortices undergo helical pairing as they are convected downstream at the same time as they experience vortex stretching because of the three-dimensionality of the flow. Once the $\bar{\omega}_3$ vortices have completed their initial roll up, a secondary instability generates the formation of the longitudinal $\bar{\omega}_{12}$ vortices. These counter-rotating vortices usually form in the braid region between adjacent $\bar{\omega}_3$ vortices and are
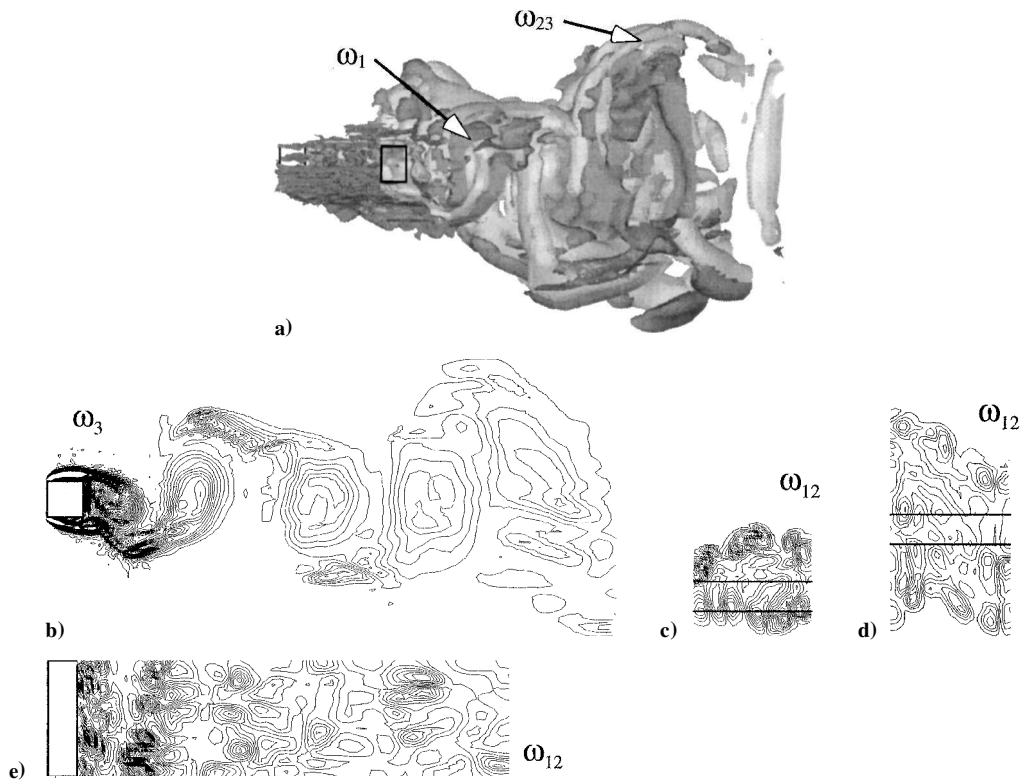
Fig. 10 Perspective view of the computational domain showing a) iso-surfaces of the spanwise $\tilde{\omega}_3$ and longitudinal $\tilde{\omega}_{12}$ vorticity at $v_0/4h$ and $v_0/2h$, respectively; and sideviews of b) the spanwise vorticity $\tilde{\omega}_3$ in $x_3/h = 0$, c) the longitudinal vorticity $\tilde{\omega}_{12}$ in $x_1/h = 2$, d) the longitudinal vorticity $\tilde{\omega}_{12}$ in $x_1/h = 8$, and e) the longitudinal vorticity $\tilde{\omega}_{12}$ in $x_2/h = 0$.
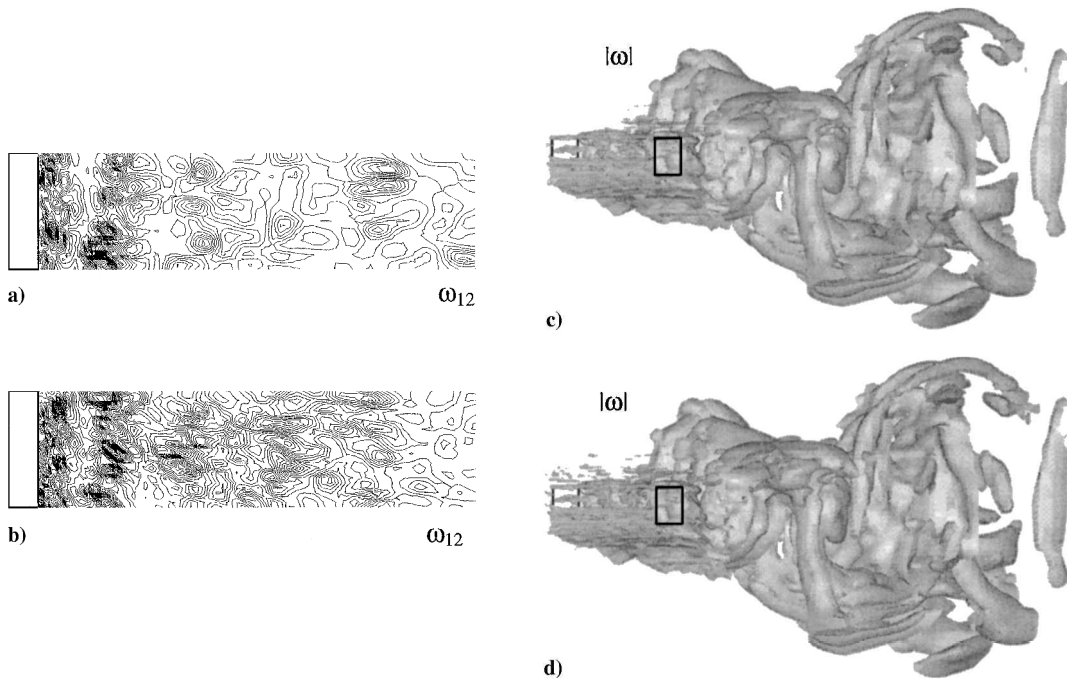

Fig. 11 Contour lines of the longitudinal $\tilde{\omega}_{12}$ vorticity in $x_2/h = 0$ from a) model A1 and b) model A2 and the corresponding iso-surfaces of the vorticity magnitude $|\tilde{\omega}|$ from c) model A1 and d) model A2.

highly coherent finger-like structures (Figs. 10a and 10c) entwining and distorting the $\bar{\omega}_3$ vortices while exchanging momentum and energy. By comparing Fig. 10b with Figs. 10c and 10d, the observation can be made that the $\bar{\omega}_3$ vortices lose their coherence after about two roll ups, whereas the longitudinal $\bar{\omega}_{12}$ vortices maintain their coherence farther downstream.

The influence of the SGS model on the resolved vorticity occurs by the $\frac{1}{2}\text{curl}(\text{div}\boldsymbol{B}_D)$ term in the vorticity equation (9). In this

paragraph a qualitative discussion of the differences observed in the vorticity fields obtained with models A1 and A2 will be given. Figures 11a and 11b show contour lines of the longitudinal vorticity $\bar{\omega}_{12}$ in the horizontal plane $x_2/h = 0$ from LES with models A1 and A2, respectively. Hence, $\bar{\omega}_{12}$ contours from model A2 exhibit smaller vortices with sharper vorticity gradients as compared to model A1. In the LES with model A1, constant vorticity structures display larger, and somewhat more organized, structures than

CDFs of |ω|
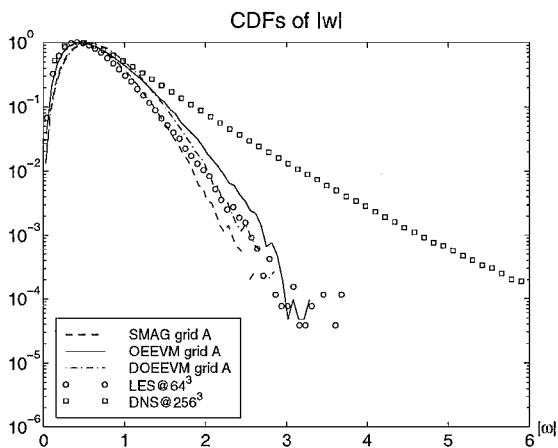
Fig. 12 PDF of the vorticity magnitude $|\bar{\omega}|$ in a subvolume extracted in the near-wake region as compared to 512^3 DNS (Ref. 33) and 64^3 LES (Ref. 34) of forced homogeneous isotropic turbulence at $Re_T = 96$ and 305.

with the dynamic model, i.e. model A2. Moreover, the breakup of spanwise vortical structures just described is visible in the spanwise vorticity contours of Fig. 10b. The LES with model A2 shows a quasi-regular pattern of $\bar{\omega}_3$ vortices spanning the full homogeneous direction. With model A1 these structures have been altered by smaller structures. By comparing iso-surfaces of the vorticity magnitude $|\bar{\omega}|$, Figs. 11c and 11d, $\bar{\omega}_{12}$ vortices of about the same diameter seem to connect the $\bar{\omega}_3$ vortices. However, at higher levels of vorticity the $\bar{\omega}_{12}$ structures are thinner for model A2. In the near wake the $\bar{\omega}_{12}$ vortices appear as slender, coherent ribs extending from one $\bar{\omega}_3$ vortex core to the next with model A2. On the contrary, structures resulting from model A1 are shorter ribs that diffuse with downstream direction. This indicates that the $\bar{\omega}_{12}$ structures have gained in strength with the dynamic model, being less diffusive than the constant coefficient model, model A1.

To give a quantitative measure of the importance of the SGS model on the resolvable vorticity, we compare, in Fig. 12, probability density functions (PDF) of $|\bar{\omega}|$, evaluated in subvolumes in the near-wake region, for models A1, A2, B1, and B3 on grid A with PDFs from 512^3 DNS (Ref. 33) and 64^3 LES (Ref. 34) of forced homogeneous isotropic turbulence. For subvolumes $|\bar{\omega}|$ is scaled with its rms value $|\bar{\omega}|_{rms}$ based on velocity data over the time interval of $2h/v_0$. A difference between the data considered here and data from homogeneous isotropic turbulence relates to the behavior of the PDFs of $|\bar{\omega}|$ for small values; because the environment of the wake involves mainly irrotational fluid, probabilities of small values of $|\bar{\omega}|$ (e.g., of $|\bar{\omega}| < 0.5$) appear as the largest for the wake data—in contrast to the smaller probabilities from the homogenous turbulence. For larger $|\bar{\omega}|$ PDFs, based on both the homogeneous turbulence and the wake data, show similar monotonically decreasing trends including the range $1 < |\bar{\omega}| < 3$, where the slopes of the PDFs are independent of the Reynolds number and tend to coincide. Figure 12 presents similar PDFs of $|\bar{\omega}|$ for the LES models, which also agree reasonably well with the PDFs of the homogeneous turbulence data indicating that the vorticity statistics from LES appear mainly unaffected by the details of the SGS model despite the differences in the vorticity distribution just discussed. Most of the region is occupied by weak vorticity with intense vorticity regions, corresponding to the $\bar{\omega}_{12}$ and $\bar{\omega}_3$ structures intermittently passing a given point in the wake, amounting to a limited fraction of the volume.

IX. Conclusion

In this study LES is used to analyze the flow around a square prism in a rectilinear channel at a prism-height Reynolds number of 2.14×10^4. Constant coefficient and dynamic algebraic and one-equation eddy-viscosity SGS models have been used to close the LES equations and to parameterize the effects of the unresolved flow on the resolvable flow structures. Moreover, three different computational grids using different resolutions are used to investigate the effects of spatial resolution on the first- and second-order statistical

moments of the velocity. For comparison, two-dimensional transient simulations using similar grids were also performed with conventional RAS models, using the k-ε and the LRR differential stress models.

Results from first- and second-order statistical moments of the resolvable velocity were validated against the measurement data of Lyn et al.[24] and of Durao et al.[25] and compared with the results from the three RAS models. From this comparison it is evident that all LES models can accurately predict the first- and second-order statistical moments of the velocity and global parameters such as the Strouhal number, the lift and drag coefficients and their fluctuations, as well as the length of the recirculation region. However, to predict correctly the maximum velocity in the recirculation region, local grid refinement in the immediate vicinity of the prism and in the recirculation region is required. In addition, the LES results appeared to be relatively independent of the details of the SGS model employed, suggesting that some features of the inertial subrange might be independent of the exact nature of small-scale turbulent dissipation, giving further confirmation of the alleged resiliency of LES to the specifics of the SGS modeling.

With the intent to further validate the LES models and to increase our present understanding of unsteady flow around a square prism, the phase-averaged flow is compared with experimental data. The qualitative features observed in the velocity field and in the normal and shear stresses essentially agree with experimental observations, although quantitative comparisons showed some differences in, e.g., the decay of the periodic stress components. This comparison supports the general belief in LES as a reliable and accurate method for studying unsteady flows. Two important features of the near wake, first suggested by Lyn et al.,[24] are supported by these simulation results: a double peak in the shear-stress distribution associated with a vortex structure is found in the near wake. The other feature concerns the possible importance of turbulence production in regions close to the vortex core because of large values of the normal Reynolds stresses. This may help in explaining the first feature, although nonlocal effects may also be important.

The instantaneous flow is also investigated to gain additional insight into the vortex dynamics and how the evolution of resolvable vorticity is affected by the SGS models. The vorticity is concentrated in elongated vortices, which are initiated by Kelvin–Helmholz instabilities, from which the primary spanwise vortical structures develop, from which in turn the longitudinal vortices develop through vortex merger and reconnection. Dynamic SGS models seem to produce more intense vortical structures than similar nondynamic models; at present this is belived to be caused by the large local variations of the model coefficients in the dynamic models. This is also apparent from the topology of the instantaneous iso-surfaces of the SGS viscosity.

References

[1] Kiya, M., and Sasaki, K., "Structure of a Turbulent Separation Bubble," *Journal of Fluid Mechanics*, Vol. 137, 1983, pp. 83–114.

[2] Cherry, N. J., Hillier, R., and Hillier, M. E. M. P., "Unsteady Measurements in a Separated and Reattaching Flow," *Journal of Fluid Mechanics*, Vol. 197, 1984, pp. 439–468.

[3] Lions, P. L., *Mathematical Topics in Fluid Mechanics*, Oxford Science Publications, Oxford, 1996, pp. 1–16.

[4] Speziale, C. G., "Analytical Methods for the Development of Reynolds-Stress Closures in Turbulence," *Annual Review of Fluid Mechanics*, Vol. 23, 1991, pp. 105–157.

[5] Lumley, J. L., "Turbulence Modelling," *Journal of Applied Mechanics*, Vol. 50, Dec. 1983, pp. 1097–1103.

[6] Galperin, B, and Orszag, S. A. (eds.), *Large Eddy Simulation of Complex Engineering and Geophysical Flows*, Cambridge Univ. Press, Cambridge, England, U.K., 1993.

[7] Rogallo, R. S., and Moin, P., "Numerical Simulation of Turbulent Flows," *Annual Review of Fluid Mechanics*, Vol. 16, 1984, pp. 99–137.

[8] Metais, O., and Lesieur, M., "Spectral Large Eddy Simulations of Isotropic and Stably Stratified Turbulence," *Journal of Fluid Mechanics*, Vol. 239, June 1992, pp. 157–194.

[9]Boris, J. P., Grinstein, F. F., Oran, E. S., and Kolbe, R. J., "New Insights into Large Eddy Simulation," *Fluid Dynamics Research*, Vol. 10, No. 4–6, 1992, pp. 199–227.

[10]Fureby, C., and Tabor, G., "Mathematical and Physical Constraints on Large Eddy Simulations," *Journal of Theoretical Fluid Dynamics*, Vol. 9, No. 2, 1997, pp. 85–102.

[11]Ghosal, S., and Moin, P., "The Basic Equations for the Large Eddy Simulation of Turbulent Flows in Complex Geometries," *Journal of Computational Physics*, Vol. 118, No. 1, 1995, pp. 24–37.

[12]Ghosal, S., "An Analysis of Numerical Errors in Large-Eddy Simulations of Turbulence," *Journal of Computational Physics*, Vol. 125, No. 1, 1996, pp. 187–206.

[13]Speziale, C. G., "Galilean Invariance of Sub Grid Scale Stress Models in Large Eddy Simulations of Turbulence," *Journal of Fluid Mechanics*, Vol. 156, July 1985, pp. 55–62.

[14]Vreman, B., Geurts, B., and Kuerten, H., "Realizability Conditions for the Turbulent Stress Tensor in Large Eddy Simulation," *Journal of Fluid Mechanics*, Vol. 278, Nov. 1994, pp. 351–362.

[15]Smagorinsky, J., "General Circulation Experiments with the Primitive Equations. I. The Basic Experiment," *Monthly Weather Review*, Vol. 91, No. 3, 1963, pp. 99–164.

[16]Lilly, D. K., "On the Application of the Eddy-Viscosity Concept in the Inertial Sub-Range of Turbulence," National Center for Atmospheric Research, NCAR Manuscript 123, Boulder, CO, 1966.

[17]Germano, M., Piomelli, U., Moin, P., and Cabot, W. H., "A Dynamic Sub Grid Scale Eddy-Viscosity Model," *Physics of Fluids A*, Vol. 3, No. 7, 1991, pp. 1760–1765.

[18]Yoshizawa, A., "Statistical Theory for Compressible Shear Flows, with the Application to Sub-grid Modelling," *Physics of Fluids A*, Vol. 29, No. 7, 1986, pp. 2152–2163.

[19]Kim, W.-W., and Menon, S., "A New Dynamic One Equation Sub Grid Scale Model for Large Eddy Simulations," AIAA Paper 95-0356, 1995.

[20]Ghosal, S., Lund, T. S., Moin, P., and Akselvoll, K., "A Dynamic Localization Model for Large Eddy Simulation of Turbulent Flows," *Journal of Fluid Mechanics*, Vol. 286, 1992, pp. 229–253.

[21]Erlebacher, G., Hussaini, M. Y., Speziale, C. G., and Zang, T. A., "Towards the Large Eddy Simulation of Compressible Turbulent Flows," *Journal of Fluid Mechanics*, Vol. 238, May 1992, pp. 155–185.

[22]Rhie, C. M., and Chow, W. L., "A Numerical Study of the Turbulent Flow past an Isolated Airfoil with Trailing Edge Separation," *AIAA Journal*, Vol. 21, No. 7, 1983, pp. 1225–1232.

[23]Fletcher, C. A. J., *Computational Methods in Fluid Dynamics*, Springer–Verlag, Berlin, 1992, pp. 242–244.

[24]Lyn, D. A., Einav, S., Rodi, W., and Park, J. H., "A Laser-Doppler Velocimetry Study of Ensemble Averaged Characteristics of the Turbulent Near-Wake of a Square Cylinder," *Journal of Fluid Mechanics*, Vol. 304, 1995, pp. 285–319.

[25]Durao, D. F. G., Heitor, M. V., and Pereira, J. C., "Measurements of Turbulent and Periodic Flows Around a Square Cross-Section Cylinder," *Experiments in Fluids*, Vol. 6, April 1988, pp. 298–304.

[26]Arnal, M., and Friedrich, R., "Large Eddy Simulation of a Turbulent Flow with Separation," *Turbulent Shear Flows 8*, edited by F. Durst, R. Friedrich, and B. Launder, Springer–Verlag, Berlin, 1993, p. 169.

[27]Silveira Neto, A., Grand, D., Métais, O., and Lesieur, M., "A Numerical Investigation of the Coherent Vortices in Turbulence Behind a Backward Facing-Step," *Journal of Fluid Mechanics*, Vol. 256, 1993, pp. 1–25.

[28]Rodi, W., Ferziger, J. H., Breuer, M., and Pourquié, M., *Proceedings from the Workshop on Large Eddy Simulation of Flows Past Bluff Bodies*, Rottach-Egern, Tegernsee, Germany, 1995.

[29]Launder, B. E., Reece, G. J., and Rodi, W., "Progress in the Development of a Reynolds Stress Turbulence Closure," *Journal of Fluid Mechanics*, Vol. 68, 1975, pp. 537–566.

[30]Reynolds, W. C., and Hussain, A. K. M., "The Mechanics of an Organized Wave in Turbulent Shear Flow. Part 3. Theoretical Models and Comparison with Experiments," *Journal of Fluid Mechanics*, Vol. 54, 1972, pp. 263–288.

[31]von Karman, T., "Über den Mechanismus des Widerstandes den ein Bewegter Körper in Einer Flüssigkeit Erfährt," *Göttingen Nachrichten Matematiche Physik Klasse*, 1912, pp. 547–556.

[32]Cantwell, B., and Coles, D., "An Experimental Study of Entrainment and Transport in the Turbulent Near Wake of a Circular Cylinder," *Journal of Fluid Mechanics*, Vol. 136, 1983, pp. 321–374.

[33]Jimenez, J., Wray, A., Saffman, P., and Rogallo, R., "The Structure of Intense Vorticity in Isotropic Turbulence," *Journal of Fluid Mechanics*, Vol. 255, Oct. 1993, pp. 65–90.

[34]Fureby, C., Tabor, G., Weller, H. G., and Gosman, A. D., "A Comparative Study of Sub Grid Scale Models in Isotropic Homogeneous Turbulence," *Physics of Fluids*, Vol. 9, No. 5, 1997, pp. 1416–1429.

R. M. C. So
Associate Editor